

---

# DYNAMIC CONTROL OF SPONTANEOUS EMISSION USING MAGNETIZED InSb HIGHER-ORDER-MODE ANTENNAS

---

Sina Aghili<sup>1</sup>, Rasoul Alaei<sup>2,3</sup>, Amirreza Ahmadnejad<sup>4</sup>, Ehsan Mobini<sup>2</sup>, Mohamadreza Mohamadpour<sup>4</sup>, Carsten Rockstuhl<sup>3,5</sup>, Robert W. Boyd<sup>2,6</sup>, and Ksenia Dolgaleva<sup>1,2</sup>

<sup>1</sup>School of Electrical Engineering and Computer Science, University of Ottawa, Ottawa, Ontario, K1N 6N5, Canada

<sup>2</sup>Department of Physics, University of Ottawa, Ottawa, Ontario K1N 6N5, Canada

<sup>3</sup>Karlsruhe Institute of Technology, Institute of Theoretical Solid State Physics, D-76131 Karlsruhe, Germany

<sup>4</sup>Department of Electrical Engineering, Sharif University of Technology, Tehran 11155-4365, Iran

<sup>5</sup>Institute of Nanotechnology, Karlsruhe Institute of Technology, D-76344 Eggenstein-Leopoldshafen, Germany

<sup>6</sup>The Institute of Optics, University of Rochester, Rochester, New York 14627, United States

## ABSTRACT

We exploit InSb's magnetic-induced optical properties to propose THz sub-wavelength antenna designs that actively tune the radiative decay rates of dipole emitters at their proximity. The proposed designs include a spherical InSb antenna and a cylindrical Si-InSb hybrid antenna that demonstrate distinct behaviors; the former dramatically enhances both radiative and non-radiative decay rates in the epsilon-near-zero region due to the dominant contribution of the Zeeman splitting electric octupole mode. The latter realizes significant radiative decay rate enhancement via magnetic octupole mode, mitigating the quenching process and accelerating the photon production rate. A deep learning-based optimization of emitter positioning further enhances the quantum efficiency of the proposed hybrid system. These novel mechanisms are potentially promising for tunable THz single-photon sources in integrated quantum networks.

**Keywords** Active antenna, Indium Antimonide (InSb), Local density of states (LDOS), Multipole moments, Radiative decay rate, Zeeman splitting effect, III-V semiconductors

## 1 Introduction

It has been long appreciated that the local density of states (LDOS), as seen by a quantum emitter, can be altered in a structured electromagnetic environment [1, 2]. The spontaneous emission (SE) rate and transition dipole strength, as the functional characteristics of a quantum emitter, greatly rely on LDOS variations [3]. In simple terms, the electric or magnetic dipole transition of quantum emitters, when considered as two-level systems, can couple to photonic resonances. Then, the enhancement of the LDOS, thanks to the structured photonic environment, accelerates the spontaneous transition rates of the quantum emitter. The SE rate enhancement is of great interest to diverse applications, including quantum source emission engineering [4, 5, 6], ultra-brighter optoelectronic devices [7, 8, 9, 10], enhanced light-matter interaction for fluorescence spectroscopy [11, 12, 13], and single-photon sources (SPSs) [14, 15, 16].

Optical resonators are high-potential devices that can serve as the structured electromagnetic media for quantum emitters by providing an enhanced LDOS [17, 18]. Radiative coupling channels emerge in a coupled emitter-resonator system, allowing one to improve the SE rate of the quantum emitter. Microcavities [19], photonic crystals, and hyperbolic metamaterials (HMMs) [20, 21, 22] are closed-cavity platforms that have been intensively investigated for their potential to increase the SE rate of quantum emitters. In recent decades, optical antennas have been the subject of this extensive research. Optical antennas are open resonators composed of sub-wavelength dielectric or metallic elements that transfer the energy of their resonance modes to quantum emitters via radiative and non-radiative channels [23, 24, 25]. Enhanced light-matter interaction at the deep sub-wavelength scale is the distinguishing advantage of antennas over cavities, leading to LDOS enhancement of quantum emitters in the coupled emitter-antenna systems. In this direction, metallic

antennas enable one to modify the SE rate of quantum emitters due to the high near-field enhancement attained by localized surface plasmon resonances (LSPRs) [26, 27, 28, 29, 30]. Metallic nanorods [31] and ring resonators [32] are highly effective plasmonic subwavelength antennas for enhancing the SE rate of quantum emitters through the excitation of LSPRs, including transversal and longitudinal plasmonic modes in nanorods, and concurrent electric and magnetic resonant modes in ring resonators. In general, coupled emitter-plasmonic antenna systems usually introduce dominant non-radiative channels due to high Joule heating losses of metallic building blocks, resulting in low quantum efficiency for the coupled systems.

Alternative designs have been investigated to mitigate dissipation losses of plasmonic antennas. Interestingly, it was shown that plasmonic devices using a dielectric spacer could avoid or limit non-radiative decay channels [33]. This idea has flourished by employing dielectric optical antennas in a wide range of applications such as surface-enhanced Raman spectroscopy [34], surface-enhanced fluorescence [35], directional light emission [36], nonlinear processes [37], and Huygens sources [38]. Furthermore, optically induced electric and magnetic Mie resonances make high-index dielectric antennas capable of efficiently engineering the SE rate of quantum emitters with electric or magnetic transition dipole moment [39, 40, 41, 42]. Besides the coexistence of electric and magnetic multipolar resonances at the sub-wavelength scale, unique characteristics such as negligible inherent losses and comparable near-field enhancement with metallic analogs enable high-index dielectric structures to suppress non-radiative channels and robustify radiative channels in the coupled emitter-dielectric antenna systems. Concentric hollow structures [43], Yagi-Uda designs [44], dimers [45], and oligomers [46] have been numerically and experimentally investigated to exhibit the high potential of dielectric sub-wavelength antennas in engineering the SE rate of quantum emitters.

Among the reported cases exploited to control the SE rate of quantum emitters for specific applications, research has been mostly limited to passive approaches such as design, material, and shape to improve the efficiency of the coupled emitter-photonic systems. Here, we aim to employ active antennas to dynamically control the SE or radiative decay rate of quantum emitters near the proposed antennas. By applying an external static magnetic field, we dynamically tune the scattering response of an optical antenna, leading to the radiative decay rate variations of a quantum emitter. In this respect, we need a material whose optical properties can be modulated upon magnetization [47]. Hence, Indium Antimonide (InSb), a III-V semiconductor with unique features of nonreciprocity, magnetoplasmonics, and magnetic tunability in the THz region [48], has been exploited to achieve an active sub-wavelength antenna. Without a static magnetic field, the scattering response of a spherical InSb antenna is divided into plasmonic, epsilon-near-zero (ENZ), and dielectric regions. By placing an electric dipole (ED) source close to the antenna as the quantum emitter, we observe different types of electromagnetic behaviors in the coupled emitter-antenna system. Non-radiative channels dominate the plasmonic region due to inherent losses of InSb below the plasma frequency, resulting in the quenching process. A transparency window corresponds to the ENZ region; hence, the quantum emitter does not experience the impact of the antenna. The coexistence of electric and magnetic multipolar resonances is observed in the dielectric region, leading to the radiative decay rate enhancement associated with dominant radiative channels. In the presence of the static magnetic field, the scattering characteristics of the InSb antenna are dramatically changed. The quenching effect becomes much more intense in the plasmonic region. Therefore, the radiative decay rate is negligible compared to the non-radiative one. The ENZ region completely disappears due to the Zeeman-splitting effect of plasmonic modes, and the quantum emitter experiences considerable radiative decay rate variations compared to the unmagnetized case. Despite dynamic control of the emission characteristics of the ED emitter via the magnetized InSb antenna, dominant non-radiative processes degrade the efficiency of the proposed antenna across the studied spectral range. To solve this limitation, as the next step, a hybrid dielectric antenna composed of Silicon (Si) and InSb layers has been proposed to serve as the high-index dielectric antenna, leading to a high radiative decay rate enhancement for the coupled magnetic dipole (MD) and ED emitter-antenna systems. Dual-band SE rate enhancement, robust magnetic response, and high quantum efficiency are important advantages realized by the magnetized hybrid antenna, opening up a possibility for the emergence of tunable magnetic SPSs.

## 2 Methodology

The spontaneous decay of a two-level system, the so-called quantum emitter, is a radiating process at a quantum level that can be estimated by Fermi's golden rule [49]. When we consider the interaction of quantum emitters with optical antennas as open resonators and lossy media, the normalized total decay rate ( $\Gamma_{\text{tot}}/\Gamma_0$ ) must be defined by LDOS in the form of [49]

$$\frac{\Gamma_{\text{tot}}}{\Gamma_0} = \frac{\rho_n(\mathbf{r}_0, \omega)}{\rho_0(\mathbf{r}_0, \omega)} = \frac{\mathbf{n}_p^T \text{Im} \left[ \overleftrightarrow{\mathbf{G}}_s(\mathbf{r}_0, \mathbf{r}_0; \omega) + \overleftrightarrow{\mathbf{G}}_0(\mathbf{r}_0, \mathbf{r}_0; \omega) \right] \mathbf{n}_p}{\mathbf{n}_p^T \text{Im} \left[ \overleftrightarrow{\mathbf{G}}_0(\mathbf{r}_0, \mathbf{r}_0; \omega) \right] \mathbf{n}_p}, \quad (1)$$

where  $\rho_n(\mathbf{r}_0, \omega)$  and  $\rho_0(\mathbf{r}_0, \omega)$  represent the LDOS at the position  $\mathbf{r}_0$  of the quantum emitter with a transition frequency  $\omega$  in the presence and absence of the optical sub-wavelength antenna, respectively. The LDOS at the position of the quantum emitter is computed using the imaginary part of the Green function [23], and  $\mathbf{n}_p$  indicates the polarization's unit vector. Without the antenna, the LDOS only depends on the electromagnetic field generated by the quantum emitter ( $\vec{\mathbf{G}}_0(\mathbf{r}_0, \mathbf{r}_0; \omega)$ ) at its position. Besides the self-generated field, in the presence of the antenna, the LDOS has another contribution from the electromagnetic field scattered by the antenna ( $\vec{\mathbf{G}}_s(\mathbf{r}_0, \mathbf{r}_0; \omega)$ ) at the emitter position, showing the impact of the local field provided by optical sub-wavelength antennas on the total decay rate modification. The contribution of the LDOS to engineering the decay rates of a quantum emitter is a common point of classical and quantum electrodynamics [49]. From a classical point of view, a quantum emitter can be modeled by a point-like dipole as an oscillating current source located near an antenna. Both electro-dynamical and classical approaches agree when the intrinsic quantum yield of the point-like quantum source is unity. The total decay rate is defined as the ratio of the total emitted power of a dipole source in the presence of the antenna to its total emitted power in the absence of the antenna, in free space, in the form of

$$\frac{\Gamma_{\text{tot}}}{\Gamma_0} = \frac{\Gamma_r + \Gamma_{\text{nr}}}{\Gamma_0} = \frac{P_r + P_{\text{nr}}}{P_0}, \quad (2)$$

where radiative and non-radiative decay rates are denoted by  $\Gamma_r$  and  $\Gamma_{\text{nr}}$ , respectively. Here,  $P_r$  and  $P_{\text{nr}}$  are also the scattered and absorbed powers by the antenna, respectively. The part of the total power incident on the antenna decays into the non-radiative channel due to the inherent losses of the antenna [49, 23]. The remaining fraction of the radiation escapes from the coupled emitter-antenna system to free space as far-field radiation. It is thus necessary to calculate the corresponding powers represented in Eq. (2) using the Poynting theorem [50]. The total emitted power is obtained by integrating the Poynting vector flux over a surface enclosing the dipole source without the antenna. The far-field radiation of the coupled emitter-antenna system is computed by placing a Poynting vector surface integral around the entire system. The dissipated power is proportional to the power loss density, determined by a volume integral around the antenna. In this study, we use COMSOL Multiphysics RF module package 6 to numerically compute the coupled emitter-antenna system's power rates corresponding to the dipole source's total decay rate [51, 52]. Owing to the inherent duality in classical electrodynamics, particularly in Maxwell's equations, the far-field radiation patterns of a quantum emitter possessing a transition magnetic dipole (MD) moment are indistinguishable from those with an electric dipole (ED) moment. Consequently, the same numerical Poynting theorem applicable for EDs can be employed within COMSOL's RF module to compute the total decay rate of an MD emitter. The distinction lies in the necessity to define a point source with a transition MD moment within the simulation model.

### 3 Results

The primary purpose of this study is to investigate how a static magnetic field applied to an optical antenna dynamically modifies the radiative decay rate of a dipole emitter in the weak-coupling regime. We first consider a spherical InSb antenna embedded in free space to serve as a sub-wavelength THz antenna. The antenna's radius is set to  $30 \mu\text{m}$ , which corresponds to the operation frequency range of 1.2 to 3 THz, matching the range of InSb's plasma frequency. The antenna's geometry and frequency range are chosen such that it can support multipolar electromagnetic resonance modes. The dielectric permittivity of InSb becomes anisotropic upon magnetic excitation perpendicular to the incidence plane, enabling the Zeeman-splitting effects on the electronic energy levels of the material proportional to the cyclotron frequency of  $\omega_c = eB/m^*$  depending on the external magnetic field ( $B$ ), electron charge ( $e$ ) and effective mass of the n-doped InSb ( $m^* = 0.0142m_0$ ).[53] (See supporting information for more detail.)

To gain insight into the light interaction with InSb semiconductor, we evaluate the scattering characteristics of the proposed antenna using multipolar decomposition [54]. We consider a linearly  $x$ -polarized plane wave with the wave vector  $\mathbf{k}$  propagating along the  $y$ -direction as illumination. By applying a static magnetic field along the  $z$ -direction, we induce anisotropy in the dielectric permittivity of InSb, thereby dynamically modifying the scattered-light characteristics (See Fig. S1 ).

As shown in Fig. 1(a), the magnetically induced anisotropy lifts the mode degeneracy, leading to separated plasmonic resonances in the magnetized InSb antenna at frequencies lower than and around  $\omega_p$ . The Zeeman-splitting effect results in new resonant modes whose spectral positions can be predicted [53]. These atomic energy level splits are linearly proportional to the Bohr magneton for weak magnetic fields. In the presence of the magnetic field  $B_z = 0.2\text{T}$ , a narrow linewidth electric octupole (EO) resonance at  $\omega/\omega_p = 0.951$  splits into multi-band EO resonances, where a peak at  $\omega/\omega_p = 1.055$  considerably amplifies the antenna's scattering response. The magnitudes of the EO resonances have been multiplied by ten to emphasize their critical role in the radiated power, as shown in Fig. 1(a,b). A parent electric quadrupole (EQ) mode at  $\omega/\omega_p = 0.94$  is split into two distinct EQ resonances at  $\omega_{-,EQ}/\omega_p = 0.84$  and

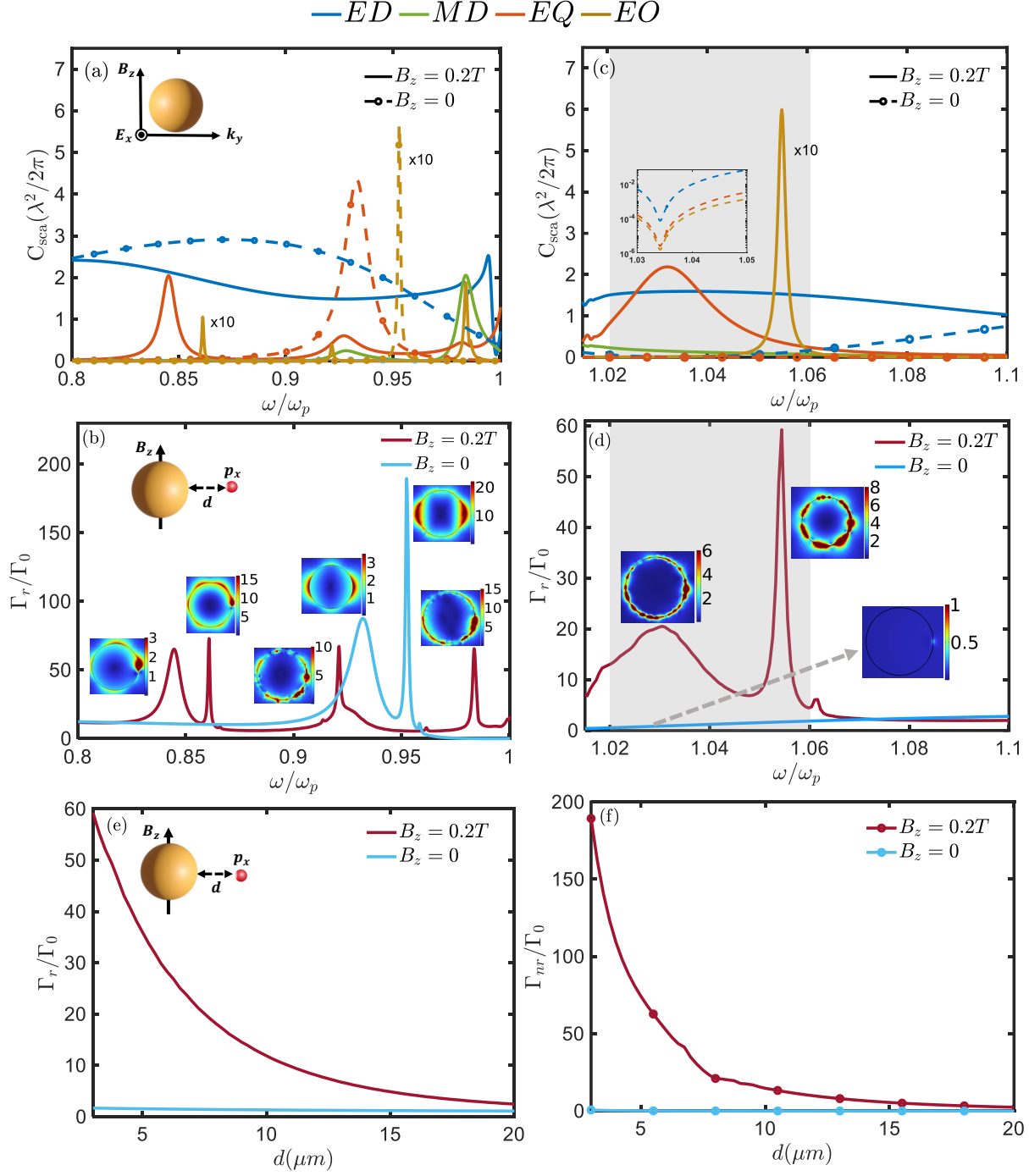


Figure 1: (a, b) The comparison of SCS spectra of the spherical InSb antenna in the presence (solid lines) and absence (dashed lines) of the static magnetic field. The external magnetic field ( $B_z = 0.2T$ ) is applied along the  $z$ -direction to dynamically modify the scattering characteristics of the antenna in the plasmonic (a) and ENZ (b) regions. (c, d) The spectral features of the radiative decay rate of the  $x$ -oriented ED source, which is placed at a distance of  $d = 3 \mu m$  from the antenna. (c) For frequencies lower than  $\omega_p$ , the coupled system realizes an enhanced multi-band radiative decay rate upon magnetization, while the unmagnetized case demonstrates a larger enhancement factor in a single band. (d) Due to the presence of Zeeman-splitting resonances, the radiative decay rate significantly improves in the ENZ region, highlighted by the gray area. The insets are the normalized electric-field distributions around the coupled emitter-antenna system, displaying how the ED source excites electric resonant modes of the antenna through the radiative coupling channels. Variations of the radiative (e) and non-radiative (f) decay rates as a function of coupling distance ( $d$ ) at the fixed frequency of  $\omega/\omega_p = 1.05$ .

$\omega_{+,EQ}/\omega_p = 1.035$ . Moreover, a broad electric dipole (ED) mode is also split into resonances at  $\omega_{-,ED}/\omega_p = 0.8$  and  $\omega_{+,ED}/\omega_p = 0.99$ . Contrary to the unmagnetized scenario, when an applied magnetic field couples with localized surface plasmon resonances, it can excite magneto-plasmonic modes. This results in the contribution of magnetic dipole (MD) resonances to the antenna's spectral response, as depicted in Fig. 1(a,b). The unmagnetized InSb antenna also experiences a plasmonic-to-ENZ transition response at frequencies slightly higher than  $\omega_p$ . This electromagnetic behavior provides invisibility, highlighted by a gray box in Fig. 1(b). The inset depicts the minimum contributions of the multipoles, leading to an almost negligible scattering response, rendering the antenna nearly invisible. In the presence of the magnetic field  $B_z = 0.2\text{T}$ , the electromagnetic response of the antenna supports a strong splitting of the EQ mode at  $\omega/\omega_p = 1.035$  and a high  $Q$  EO mode at  $\omega/\omega_p = 1.055$ , leading to a transition from invisibility to visibility associated with a 60-fold enhancement of the total scattering cross section (SCS). Besides the splitting of the EQ and EO modes, broadband ED and MD resonances also contribute to the SCS of the magnetized InSb antenna.

The contribution of the LDOS to the total decay rate of a quantum emitter implies that local electric field enhancement provided by the plasmonic characteristic of the InSb antenna significantly improves the radiative decay rate of a coupled emitter to the antenna. Such a unique feature motivates us to study the dynamic engineering of a dipole emitter's radiative decay rate in microscale proximity to the spherical InSb antenna beyond a quasi-static approximation.

Figures 1(c,d) depict the dependence of the radiative decay rate on frequency, where the InSb antenna is fed by an  $x$ -oriented ED source with the separation distance of  $d = 3 \mu\text{m}$ . The excited resonant modes of the antenna highly rely on the orientation and nature of the emitter [55]. Without the magnetic field, as shown in Fig. 1(c), the radiative decay rate witnesses a significant enhancement in the frequency range from  $\omega/\omega_p = 0.9$  to  $0.95$ , corresponding to the spectral interval of the parent EQ and EO resonances. The radiative decay rate experiences about 200 times enhancement due to the EO resonance with a high  $Q$  factor, while a broader EQ resonance leads to a lower enhancement. On the other hand, the emitter coupled to the magnetized antenna realizes multi-band radiative decay rate enhancement owing to the contribution of Zeeman-splitting EO, EQ, and ED modes to the radiative coupling channels. The mechanism of the radiative decay rate enhancement around frequencies of  $\omega/\omega_p = 0.85$  and  $0.925$  are similar to the unmagnetized case. Lower Zeeman-splitting EO and EQ modes resonantly interact with the transition moment of the ED source, realizing up to 50-fold radiative decay rate enhancement at  $\omega/\omega_p = 0.85$ . As shown in Fig. 1(c), another enhancement arises from the EO and EQ modes at  $\omega/\omega_p = 0.925$ , where the latter broadens the spectral response of the radiative decay rate. Other radiative decay rate maxima are observed at  $\omega/\omega_p = 0.98$ , resulting from the higher Zeeman-splitting EO resonance.

The interesting behavior of the magnetized InSb antenna is observed in Fig. 1(d), where the radiative decay rate enhances up to 60 times due to the resonant interaction of the ED source's transition moment with both the broad EQ and higher Zeeman-splitting EO modes. However, without the magnetic field, the InSb antenna is invisible, and thus the radiative decay rate is equal to one and similar to that in free space across the spectral range highlighted by the gray area. As mentioned earlier, the antenna can either radiatively or non-radiatively dissipate the emitted energy of the ED source. In the coupled emitter-antenna system, the radiative decay rate channel corresponds to the antenna's scattered electromagnetic field at the emitter position, while the non-radiative decay rate channel is proportional to the absorption losses of the antenna.

The separation distance between the antenna and the ED source called the coupling distance, is another crucial parameter modifying the total decay rate. Figure 1(e and f) indicates the distance dependence of the radiative and non-radiative decay rates at the fixed frequency of  $\omega/\omega_p = 1.05$  associated with the transparent window of the InSb antenna. Under zero magnetization, the radiative decay rate is unity, irrespective of the coupling distance, since the antenna is invisible and the surrounding electromagnetic environment evokes free space for the dipole source. By applying the static magnetic field  $B_z = 0.2\text{T}$ , Zeeman-splitting modes realize a 60-fold enhancement for the radiative decay rate when the ED source and the antenna are in close proximity. By increasing the coupling distance, the resonant interaction of splitting modes with the ED source's transition moment weakens, and thus the enhancement factor decreases. For longer distances, the enhancement factor is unity as the dipole source cannot "feel" the antenna (see Fig. 1(e)). As shown in Fig. 1(f), the unmagnetized coupled emitter-antenna experiences a zero non-radiative decay rate due to the invisibility of the antenna. Under a biased magnetic field of  $B_z = 0.2\text{T}$ , a strong near-field interaction between the ED source's transition moment and the broad ED mode of the antenna results in the Forster resonant energy transfer (FRET) effect [56], and thus the non-radiative decay rate dramatically enhances for shorter coupling distances. This non-radiative dipole-dipole interaction becomes ineffective for longer coupling distances, so the non-radiative decay rate falls to zero far from the antenna (see Fig. 1(f)). The magnetized InSb antenna acting as an active photonic device allows us to realize dynamically tunable multi-band SE rate enhancement. However, the total emitted power of the ED source is mainly absorbed by the antenna in the near-field region due to significant Joule heating losses of the InSb material, as shown in Fig. 1(f). Dominant non-radiative channels in the coupled system design give rise to a low quantum efficiency for the antenna, impairing the high free-space radiation rate required for SPSs. In the following, we propose an all-dielectric antenna featuring a high quantum efficiency.

Let us consider a hybrid cylindrical antenna composed of silicon (Si) and InSb layers with the same radii of  $r = 35 \mu\text{m}$  in the THz regime. The silicone layer, as a high-index and low-loss material, comprises the antenna's upper part with a height of  $h_1 = 80 \mu\text{m}$  to harness the Joule heating losses of the design. The dielectric permittivity of Si is set to  $\varepsilon_{\text{Si}} = 10.6$  since the material shows a constant permittivity with negligible inherent losses in the studied frequency range. The lower part is made of InSb with a height of  $h_2 = 8 \mu\text{m}$  to supply the magneto-optical properties required for this active antenna. The design principle resides on two aspects. First, the aspect ratio,  $(h_1+h_2)/r$ , of the cylindrical antenna is optimized to support scattering resonances with high  $Q$  factors [57]. Second, a given spectral range far from the main absorption band of InSb is chosen such that the material shows moderate positive dielectric permittivity and low losses, as shown in Fig. S1. When both constituent elements of the antenna exhibit dielectric behaviors, an induced displacement current exceeds the conductive one in the desired frequency range, and thus the all-dielectric antenna can excite robust concurrent electric and magnetic resonances (See Fig. S3).

In Fig. 2, we investigate the radiative decay rate variations of an emitter with ED transition, located near the hybrid antenna with the coupling distance of  $d = 3 \mu\text{m}$ . By applying an external static magnetic field, the antenna's scattering response is modified, enabling one to dynamically control the total decay rate of the coupled ED source. As a comparison, we show the SCS of the magnetized antenna under plane-wave illumination in Fig. 2(a). In the presence of a magnetic field  $B_z = 0.2\text{T}$ , a dominant narrow linewidth magnetic octupole (MO) mode is split into distinct resonances due to the Zeeman effect, while the other broadband multipole resonances experience slight blueshifts. Two MO resonances at frequencies of  $\omega_{-,MO}/\omega_p = 1.202$  and  $\omega_{+,MO}/\omega_p = 1.206$  result from a parent MO resonance at  $\omega/\omega_p = 1.204$ . Positioning the  $x$ -oriented ED source parallel to the hybrid antenna's nearest surface, specifically at the side, enhances the radiative decay rate by a factor of 20 around  $\omega/\omega_p = 1.24$ , due to the strong contribution from the broad EQ mode to the radiative coupling channels. In this configuration, the high- $Q$  MO mode has only weak coupling with the ED transition moment of the emitter, resulting in a more modest, 10-fold enhancement of the radiative factor around the resonance frequency of the MO mode (see Fig. 2(b)).

Under a biased magnetic field  $B_z = 0.2 \text{ T}$ , the coupled system retains multi-band radiative decay rate enhancement, akin to the unmagnetized case. However, the contribution of the MO splitting modes to the radiative coupling channels undergoes further attenuation due to the Zeeman effect.

Considering the significant impact of the emitter's orientation on decay-rate enhancement, we examine a configuration in which a  $z$ -oriented ED emitter is aligned parallel to the incident polarization and situated at the side position relative to the antenna, as illustrated in Fig. 2(c). Under zero magnetization, the MO mode strongly contributes to the radiative coupling channels, and the radiative decay rate experiences up to a 140-fold enhancement. As shown in Fig. 2(c), the coupled system can enhance the dual-band radiative decay rate when the magnetized antenna supports the MO splitting resonances. Insets display the normalized electric field distributions of the coupled system, allowing us to perceive the contribution of multipole moments in the coupling channels. The electric-field profiles verify that the magnetic field application only affects the spectral resonance positions, irrespective of their inherent properties.

Figure 2(d) depicts the non-radiative decay rate of the  $z$ -oriented ED source as a function of the coupling distance ( $d$ ), highlighting that the power absorbed by the antenna at the MO mode's resonance frequency, corresponding to the maximum radiative decay rate, is negligible. This stresses the proficiency of the proposed all-dielectric antenna in suppressing dissipative losses compared to its plasmonic counterpart, as evidenced by the considerably lower non-radiative decay rate relative to the radiative decay rate in the near-field region. Therefore, it is expected to have a high quantum efficiency for the magnetized hybrid antenna that can be exploited for various applications demanding high multi-band radiation.

As demonstrated in Fig. 2, a magnetic hotspot is achieved due to the MO resonance with a high  $Q$  factor, promising highly efficient control of the radiative decay rate of an MD emitter. An  $x$ -oriented MD emitter located perpendicular to the closest surface of the antenna enables the strong radiative coupling channels with the MO resonant mode in the spectral range from  $\omega/\omega_p = 1.2$  to  $1.21$ . In the coupled MD emitter-antenna system, the radiative decay rate demonstrates a 600-fold enhancement due to a narrow-linewidth MO resonance under zero-bias magnetic field that can be engineered in the presence of the applied magnetic field (See Fig. 3.(a)). Hence, selective emission is another promising advantage of the magnetized hybrid antenna in which spectral bands of the enhanced radiative decay highly depend on the applied magnetic field's strength. Increasing the applied magnetic field makes resonance peaks well-separated across a broader spectral range. The Zeeman-splitting effect is linearly proportional to the cyclotron frequency for magnetic fields  $B_z < 0.3 \text{ T}$ , and the split lines are symmetrical with respect to the original resonance peak observed at  $B_z = 0$ . For larger magnetic field values, we can not estimate the spectral position of splitting resonances based on Bohr magneton approximation, and new resonance peaks are asymmetrically separated compared to the original resonance. As demonstrated in Fig.3(b), higher-frequency splitting resonances experience considerable blue-shifts while lower ones are slightly red-shifted under a biased magnetic field larger than  $B_z = 0.3 \text{ T}$ .

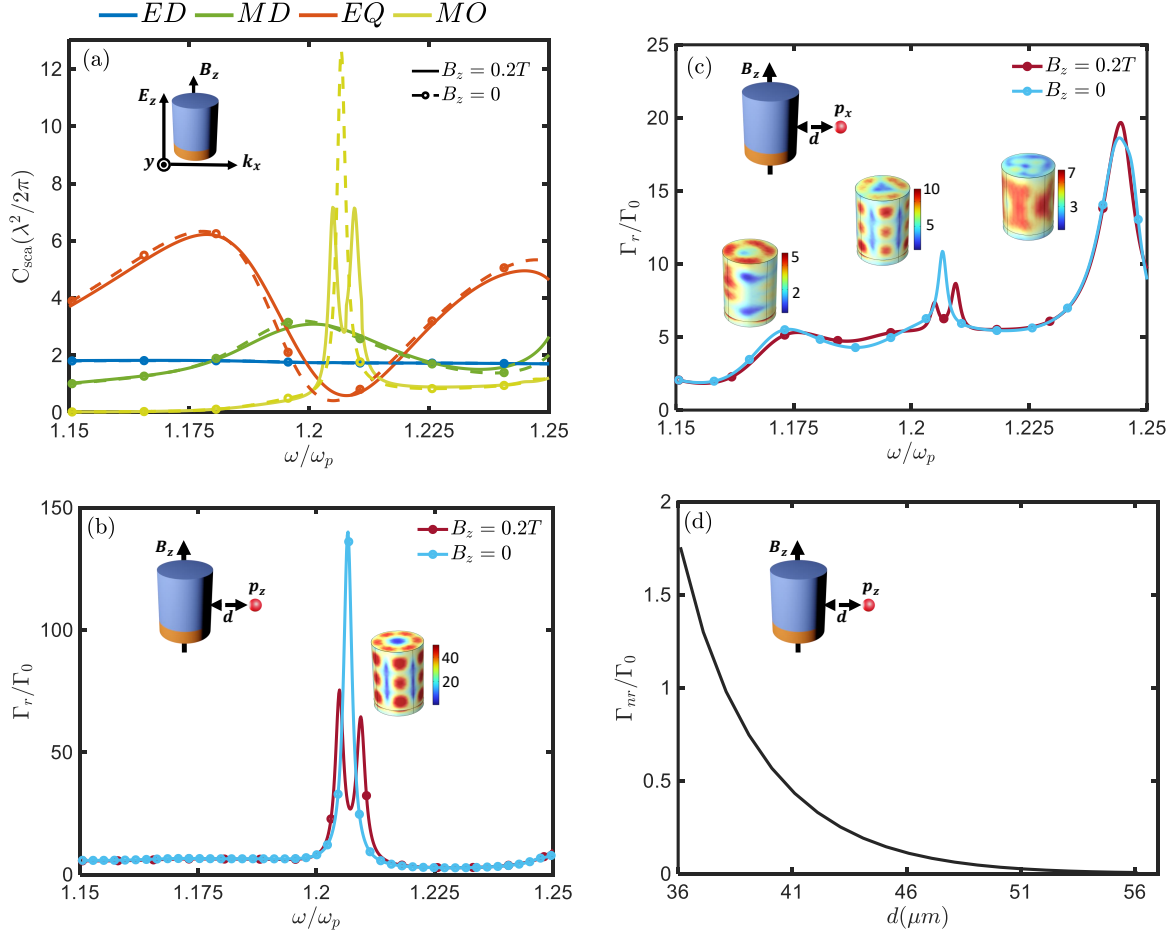


Figure 2: (a) The scattering spectra of the hybrid antenna under plane-wave illumination in the presence (solid lines) and absence (dashed lines) of the static magnetic field. By applying the static magnetic field ( $B_z = 0.2\text{ T}$ ) along the  $z$ -direction, multipole moments experience a slight redshift due to the Zeeman effect, while the high- $Q$  parent MO mode splits into two resonant modes in the spectral interval from  $\omega/\omega_p = 1.2$  to  $1.22$ . (b) The radiative decay rate of the  $x$ -oriented ED source located near the hybrid antenna with the coupling distance of  $d = 3\ \mu\text{m}$ . The spectral response of the radiative decay rate demonstrates a strong dual-band enhancement factor upon magnetization, whereas the maximum radiative decay rate enhancement is recorded under zero magnetic bias. The insets display the normalized electric-field distribution of the MO resonance peak excited by the ED emitter. (c) The enhancement of the radiative decay rate for the coupled system is driven by an  $z$ -oriented ED emitter as a function of frequency. In this orientation, every multipole moment contributes radiatively to the coupling channels. The insets, showing the normalized electric-field distributions for each resonance peak, highlight the relatively weak coupling between the multipole moments and the ED source. Spectral variations of (d) non-radiative decay rates of the magnetized system upon the  $z$ -oriented ED emitter excitation at the fixed frequency of  $\omega/\omega_p = 1.205$  corresponding to the resonance frequency of the MO mode. It clearly shows that the non-radiative decay rate of the emitter coupled to the dielectric antenna is significantly lower than that in the coupled emitter-plasmonic antenna system. In this figure, the coupling distance is set to be  $3\ \mu\text{m}$ .

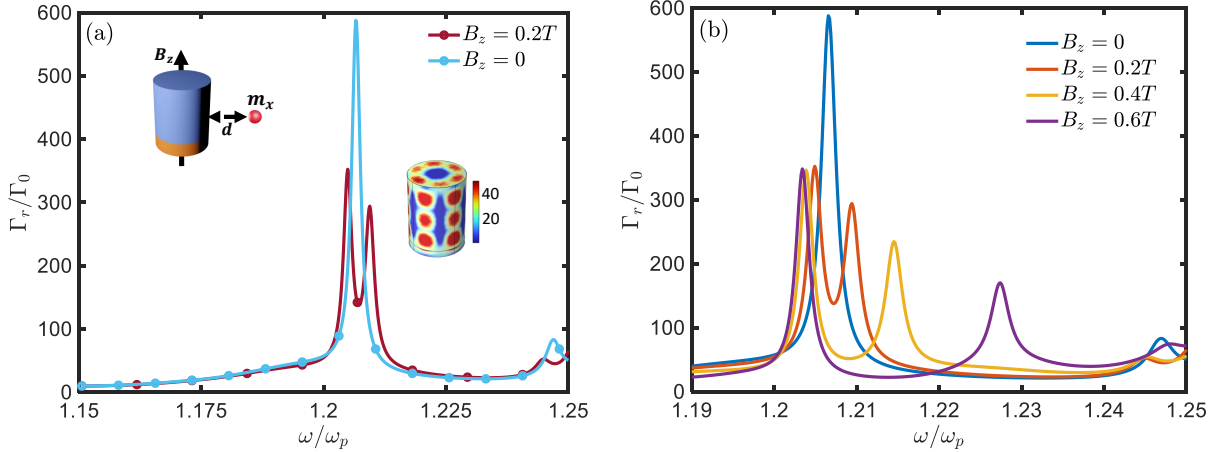


Figure 3: (a) Frequency-dependent radiative decay rate of the  $x$ -oriented MD emitter positioned near the hybrid antenna. The high- $Q$  MO resonance generates substantial radiative coupling with the emitter’s transition MD moment, leading to a 600-fold enhancement in the photon production rate. (b). Dynamically tunable dual-band radiative decay rate enhancement of the  $x$ -oriented MD source employing the applied magnetic field increment in the frequency range corresponding to the high- $Q$  MO mode.

As highlighted previously, the LDOS enhancement factor and the normalized radiative and non-radiative decay rates depend on the position, orientation, and type of the dipole source or quantum emitter. Evaluating decay rates based on varied antenna parameters presents complexity and labor intensiveness such that numerical and semi-analytical methods often ignore mutual interactions, leading to suboptimal results. To address this challenge, we employ advanced deep-learning methods recognized for navigating complex and multi-dimensional datasets. We propose a convolutional neural network (CNN) architecture [58, 59] to discern spatial intricacies within the coupled emitter-antenna system. This CNN design adopts several convolutional layers, employing Rectified Linear Unit (ReLU) activation to determine hierarchical data representations. CNN output undergoes flattening and feeds into dense layers for predictive analysis.

As illustrated in Fig. 4(a), the CNN inputs encompass the spatial coordinates of the quantum emitter, the operational frequency, the value of the applied static magnetic field, and the type of quantum emitter. The initial computational step involves the convolution layer of  $C_i = \text{ReLU}(\text{Conv}(X, W_i) + b_i)$ , where  $C_i$  determines each layer output. Here,  $X$  represents the input data,  $W_i$  is the weight matrix for the  $i^{\text{th}}$  filter, and  $b_i$  is its corresponding bias. The ReLU function introduces non-linearity, allowing the model to adjust its prediction. This operation is repeated for  $i = 1$  to  $N$ , where  $N$  is the total number of filters in the convolution layer.

The output is passed through fully connected layers, and the network undergoes a flattening process, converting the 2D data structure from the convolution layer into a 1D vector. This process of transformation is represented as  $FC = \text{ReLU}(W_{FC} \times \text{Flatten}(C_N) + b_{FC})$ , where  $W_{FC}$  represents the weight matrix and  $b_{FC}$  is the bias for the fully connected layer. The network concludes with the output layer, which uses the expression of  $\hat{Y} = W_{\text{out}} \times FC + b_{\text{out}}$ , where the output  $\hat{Y}$  demonstrates the estimated radiative or non-radiative decay rate.

Utilizing our approach, we can determine both the type and optimal positioning of a quantum emitter near an antenna to optimize radiative decay rates. Figure 4(b) illustrates the radiative decay rate for a dipole source positioned variably around the antenna’s external surface. Notably, an  $x$ -oriented MD source placed adjacent to the hybrid antenna at  $(37 \mu\text{m}, 0 \mu\text{m}, 40 \mu\text{m})$  reaches an enhancement factor of 700 at the frequency range corresponding to the MO mode’s resonance frequency under zero magnetization. To verify this prediction, Fig. 4(c) displays the simulation result of both radiative and non-radiative decay rates for  $m_x$  dipole source at its prime location, mirroring CNN’s predictive output. The inset presents the far-field radiation pattern of the maximum value corresponding to the dominant MO mode in a non-magnetized state.

## 4 Conclusion

In this study, we numerically investigated the impact of an active antenna on the total decay rate of an emitter. The active antenna enables one to manipulate its scattering response by external agents dynamically. InSb material, a III-V



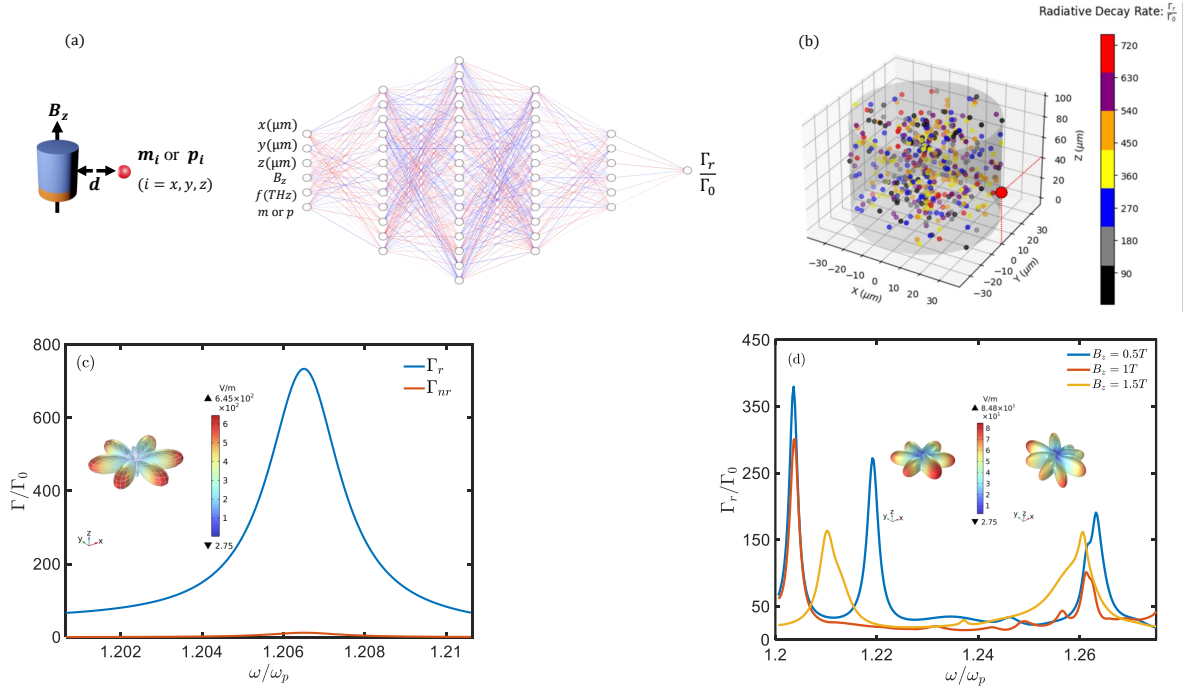


Figure 4: (a) The CNN architecture tailored to identify the ideal position of a variably oriented dipole source that yields the maximum radiative decay rate near the hybrid antenna. This approach holds the constant coupling distance ( $d = 3 \mu\text{m}$ ). (b) The radiative decay rate of the  $m_x$  dipole source at varied positions around the hybrid antenna's outer surface. The CNN prediction indicates a seven-fold enhancement factor when  $m_x$  is situated at  $(37 \mu\text{m}, 0 \mu\text{m}, 40 \mu\text{m})$  within the frequency range corresponding to the MO mode in a non-magnetized state. (c) The radiative and non-radiative decay rates of the  $m_x$  dipole source at its optimal position, aligning with the MO mode's resonant frequency in a non-magnetized environment under numerical simulation. The maximum value of the radiative decay rate validates the CNN prediction. The inset highlights the far-field radiation pattern, emphasizing the dominant radiation efficiency of the MO mode into free space. (d) The radiative decay rate variations for three different values of the applied magnetic field. The Zeeman-splitting effect becomes broader with respect to the increment in the applied magnetic field, while the enhancement factor decreases compared to the absence of the magnetic field. Insets exhibit the spatial variations of the far-field electric-field patterns corresponding to radiative decay rate maxima at the resonant frequencies of  $\omega/\omega_p = 1.207$ , ( $B_z = 1.5T$ ) and  $\omega/\omega_p = 1.264$  ( $B_z = 1T$ ).

semiconductor with strong magneto-optical properties in the THz region has been employed to realize the active antenna that can modify light-matter interaction via an applied static magnetic field. We used the multipole decomposition method to obtain the SCS of the antenna under plane-wave illumination. The scattering response of the antenna allows us to determine which type of emitters efficiently interact with the antenna. In the first section, we proposed a spherical InSb antenna to modify the radiative decay rate of an ED source upon magnetization. We have shown that the radiative decay rate experiences a multi-band enhancement when the magnetized antenna has plasmonic features, whereas the maximum enhancement factor of about 200-fold is observed for the unmagnetized case. Moreover, a transition from invisibility to visibility has been shown in the ENZ region such that the transparent antenna turns into a strong scatterer under a biased magnetic field, and thus the radiative decay rate dramatically enhances up to 60 times. However, the proposed active antenna suffers from high Joule heating losses, impairing its quantum efficiency associated with a low photon production rate. To mitigate this limitation, we proposed a cylindrical hybrid antenna composed of Si and InSb layers to act as an all-dielectric active antenna. Due to its robust magnetic resonance, we have found that the hybrid antenna is very promising for dynamic control of the radiative decay rate of an MD emitter. Results show that the magnetized hybrid antenna achieves an enhanced tunable dual-band radiative decay rate for the MD source, so each band represents several hundred-fold enhancement factors. Moreover, we have found that the hybrid antenna harnesses the non-radiative processes, leading to high quantum efficiency. Such unique features open up a possibility for tunable SPSs required in quantum information processing. Finally, we employed a modified deep-learning CNN to determine the emitter's position within the coupled system precisely. This position maximizes the radiative decay rate when an  $x$ -oriented MD source, located at coordinates  $(37 \mu\text{m}, 0 \mu\text{m}, 40 \mu\text{m})$ , couples with the hybrid antenna. Remarkably,

this configuration boosts the radiative decay rate up to 720 times under zero magnetization. This finding was further validated through numerical simulations using Comsol, confirming the prediction of our modified deep-learning network. Offering dynamic splitting bandwidth via the proposed coupled system holds significant potential for designing tunable THz single-photon sources suitable for practical quantum applications.

## Supplemental Material

### S1 Dielectric Permittivity of InSb

We use the Drude model to express the permittivity tensor of InSb at THz frequencies, denoted by

$$\varepsilon(\omega) = \begin{bmatrix} \varepsilon_{xx} & \varepsilon_{xy} & 0 \\ \varepsilon_{yx} & \varepsilon_{yy} & 0 \\ 0 & 0 & \varepsilon_{zz} \end{bmatrix}, \quad (3)$$

where the tensor elements of Eq. (3) are defined as

$$\varepsilon_{zz}(\omega) = \varepsilon_{\infty} - \frac{\omega_p^2}{\omega^2 + i\gamma_p\omega} \quad (4)$$

$$\varepsilon_{xx}(\omega) = \varepsilon_{yy}(\omega) = \varepsilon_{\infty} - \frac{\omega_p^2(\omega^2 + i\gamma_p\omega)}{(\omega^2 + i\gamma_p\omega)^2 - \omega_c^2\omega^2} \quad (5)$$

$$\varepsilon_{xy}(\omega) = -\varepsilon_{yx}(\omega) = -i \frac{\omega_p^2\omega_c\omega}{(\omega^2 + i\gamma_p\omega)^2 - \omega_c^2\omega^2}. \quad (6)$$

We consider the parameters of an n-doped InSb semiconductor [60, 47], where  $\varepsilon_{\infty} = 15.6$  is the background permittivity,  $\omega_p = 12.56 \times 10^{12} \text{rad/s}$  is the plasma frequency,  $\gamma_p = 0.01\omega_p$  as the damping constant represents the Ohmic losses of InSb, and  $\omega_c = eB_z/m^*$  is the cyclotron frequency depending on the external magnetic field ( $B_z$ ), electron charge ( $e$ ) and effective mass ( $m^* = 0.0142m_0$ ). The low effective mass of InSb results in a strong anisotropy under a weak external magnetic field [48, 47, 53]. Figure S1 compares the spectral dependency of InSb's complex permittivities in the presence and absence of the applied magnetic field.

Without the magnetic field ( $B_z = 0$ ), off-diagonal elements of the InSb permittivity disappear due to the cyclotron frequency dependence. On the other hand, diagonal elements are identical, showing negative real parts at lower frequencies than  $\omega_p$ , and positive values for the imaginary parts across the whole spectral range (Fig. S1a and c). Under zero magnetization, the optical response of InSb only depends on the real part of  $\varepsilon_{zz}(\omega)$  so that its negative values result in a plasmonic behavior [61], and the positive ones turn the material into a relatively high-index dielectric [47]. Positive values of its imaginary part demonstrate the Ohmic losses of InSb, specifically in the plasmonic region. In the presence of the magnetic field ( $B_z = 0.2\text{T}$ ), the real parts of the components remain almost unchanged, and only  $\varepsilon_{xx}(\omega)$  increases at lower frequencies compared to the previous case (Fig. S1b). On the other hand, the imaginary parts of the magnetized components experience main variations, in which off-diagonal components demonstrate the same values with different signs. As shown in Fig. S1(d),  $\varepsilon_{xy}(\omega)$  indicates negative values that can robustly demonstrate the plasmonic behavior of InSb in agreement with negative real parts of the diagonal components, whereas  $\varepsilon_{yx}(\omega)$  increases the Ohmic losses of the material in the plasmonic region due to its considerable positive values.

### S2 Scattering Cross Section of the Single Resonant Antenna

We first need to evaluate the scattering characteristics of the proposed antenna using multipolar decomposition [55]. The incident light can induce an electric conductive or displacement current on the antenna such that the scattered field originates from the induced oscillating current carrying on multipole moments mentioned in Eq. (11). The respective induced current is described as  $J(r, \omega) = i\omega\varepsilon_0(\varepsilon(\omega) - 1)E(r, \omega)$ , where  $\varepsilon(\omega)$  is the dielectric permittivity of the antenna and  $E(r, \omega)$  describes the electric field distribution around and inside the antenna that can be numerically calculated by the RF module of COMSOL version 6 software. By having the electric-induced current, we can obtain the proposed antenna's total scattering cross-section (SCS) based on the contribution of multipole moments as follows

$$p_{\alpha} = -\frac{1}{i\omega} \left[ \int J_{\alpha} dv + \frac{k^2}{10} \int (\mathbf{J} \cdot \mathbf{r}) r_{\alpha} - 2r^2 J_{\alpha} dv + \frac{k^4}{280} \int 3r^4 J_{\alpha} - 2r^2 (\mathbf{r} \cdot \mathbf{J}) r_{\alpha} dv \right], \quad (7)$$

$$m_{\alpha} = \frac{1}{2} \left[ \int (\mathbf{r} \times \mathbf{J})_{\alpha} dv - \frac{k^2}{10} \int r^2 (\mathbf{r} \times \mathbf{J})_{\alpha} dv \right], \quad (8)$$

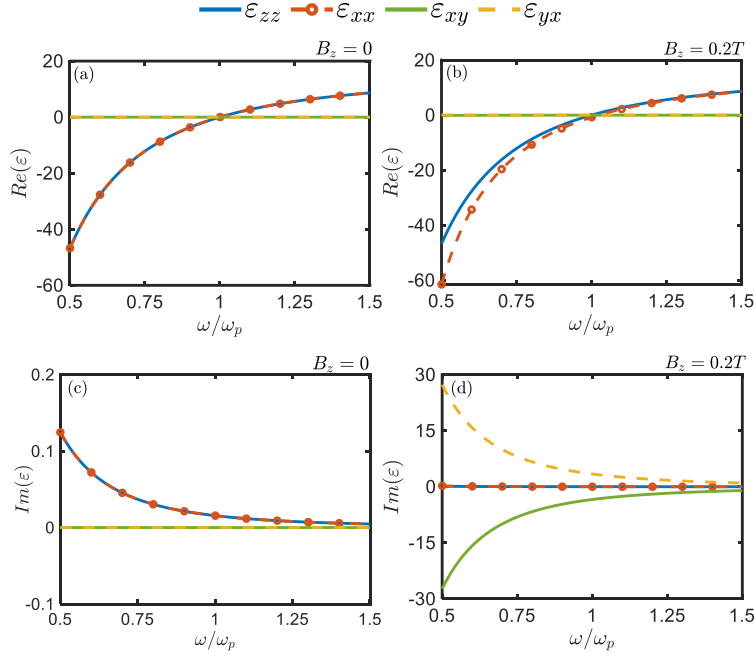


Figure S1: (a, c) Real and imaginary parts of InSb's dielectric permittivity versus frequency under zero magnetization ( $B_z = 0$ ). Diagonal elements are identical, while off-diagonal ones vanish due to cyclotron frequency dependence. (a) The real part of the diagonal elements is negative at frequencies  $\omega/\omega_p < 1$ , representing the plasmonic region of InSb. For frequencies  $\omega/\omega_p > 1$ , InSb is a dielectric material due to the positive real part of its permittivity. (c) The positive imaginary part of diagonal elements is larger in the plasmonic region, denoting the Joule heating losses of InSb as the plasmonic material. (b, d) Real and imaginary parts of InSb's permittivity as a function of frequency upon magnetization ( $B_z = 0.2T$ ). (b) The real part of diagonal elements increases compared to the unmagnetized case, and  $\varepsilon_{xx}(\omega)$  dissociates from  $\varepsilon_{zz}(\omega)$  at lower frequencies. On the other hand, off-diagonal elements remain almost unchanged, similar to the previous case. (d) In the presence of the applied magnetic field, the imaginary part of diagonal elements is negligible, while off-diagonal ones demonstrate considerable variations.  $\varepsilon_{xy}(\omega)$  shows negative values across the studied spectral range so that it improves the plasmonic behavior of InSb at frequencies  $\omega/\omega_p < 1$ . On the other hand,  $\varepsilon_{yx}(\omega)$  is positive throughout the broad spectral range, increasing absorption losses of the material.

$$Q_{\alpha\beta}^e = -\frac{1}{i\omega} \left[ \int r_\alpha J_\beta + r_\beta J_\alpha - \frac{2}{3} (\mathbf{r} \cdot \mathbf{J}) \delta_{\alpha\beta} dv + \frac{k^2}{42} \int 4 (\mathbf{r} \cdot \mathbf{J}) r_\alpha r_\beta + 2\delta_{\alpha\beta} (\mathbf{J} \cdot \mathbf{r}) r^2 - 5r^2 (r_\alpha J_\beta + r_\beta J_\alpha) dv \right], \quad (9)$$

$$Q_{\alpha\beta}^m = \frac{1}{3} \left[ \int r_\alpha (\mathbf{r} \times \mathbf{J})_\beta + r_\beta (\mathbf{r} \times \mathbf{J})_\alpha dv - \frac{k^2}{4} \int r^2 (r_\alpha (\mathbf{r} \times \mathbf{J})_\beta + r_\beta (\mathbf{r} \times \mathbf{J})_\alpha) dv \right], \quad (10)$$

$$O_{\alpha\beta\gamma}^e = -\frac{1}{i\omega} \left[ \int r_\alpha r_\beta J_\gamma + r_\beta r_\gamma J_\alpha + r_\gamma r_\alpha J_\beta - \frac{1}{5} \delta_{\alpha\beta} (r^2 J_\gamma + 2 (\mathbf{r} \cdot \mathbf{J}) r_\gamma) - \frac{1}{5} \delta_{\beta\gamma} (r^2 J_\alpha + 2 (\mathbf{r} \cdot \mathbf{J}) r_\alpha) - \frac{1}{5} \delta_{\gamma\alpha} (r^2 J_\beta + 2 (\mathbf{r} \cdot \mathbf{J}) r_\beta) dv \right], \quad (11)$$

$$O_{\alpha\beta\gamma}^m = \frac{1}{24} \left[ \int (r_\alpha r_\beta (\mathbf{r} \times \mathbf{J})_\gamma + r_\beta r_\gamma (\mathbf{r} \times \mathbf{J})_\alpha + r_\gamma r_\alpha (\mathbf{r} \times \mathbf{J})_\beta) - \frac{1}{5} \delta_{\alpha\beta} r^2 (\mathbf{r} \times \mathbf{J})_\gamma - \frac{1}{5} \delta_{\beta\gamma} r^2 (\mathbf{r} \times \mathbf{J})_\alpha - \frac{1}{5} \delta_{\gamma\alpha} r^2 (\mathbf{r} \times \mathbf{J})_\beta dv \right], \quad (12)$$

and the scattering cross-section from the antenna can be expressed in terms of multipole moments provided by Eqns. (5) to (10) as

$$C_{\text{sca}}^{\text{tot}} = \frac{k^4}{6\pi\epsilon_0^2 |E_{\text{inc}}|^2} |p_\alpha|^2 + \frac{k^4}{6\pi c^2 \epsilon_0^2 |E_{\text{inc}}|^2} |m_\alpha|^2 + \frac{k^6}{160\pi\epsilon_0^2 |E_{\text{inc}}|^2} \sum_{\alpha\beta} |Q_{\alpha\beta}^e|^2 + \frac{k^6}{80\pi c^2 \epsilon_0^2 |E_{\text{inc}}|^2} \sum_{\alpha\beta} |Q_{\alpha\beta}^m|^2 + \frac{k^8}{1890\pi\epsilon_0^2 |E_{\text{inc}}|^2} \sum_{\alpha\beta\gamma} |O_{\alpha\beta\gamma}^e|^2 + \frac{k^8}{1890\pi c^2 \epsilon_0^2 |E_{\text{inc}}|^2} \sum_{\alpha\beta\gamma} |O_{\alpha\beta\gamma}^m|^2. \quad (13)$$

Here  $p_\alpha/m_\alpha$ ,  $Q_{\alpha\beta}^e/Q_{\alpha\beta}^m$ , and  $O_{\alpha\beta\gamma}^e/O_{\alpha\beta\gamma}^m$  are electric/magnetic dipole moments, electric/magnetic quadrupole moments, and electric/magnetic octupole moments, respectively.  $c$  is the speed of light,  $E_0$  represents the electric field magnitude of the incident light, and  $\alpha, \beta, \gamma = x, y, z$ .

### B.1 Spherical InSb Antenna

We consider a linearly  $x$ -polarized plane wave propagating with the wavevector  $k$  along the  $y$ -direction as illumination. By applying a static magnetic field, we dynamically modify the scattered light characteristics of the antenna owing to the anisotropic behavior observed in InSb dielectric permittivity (See Fig. 1).

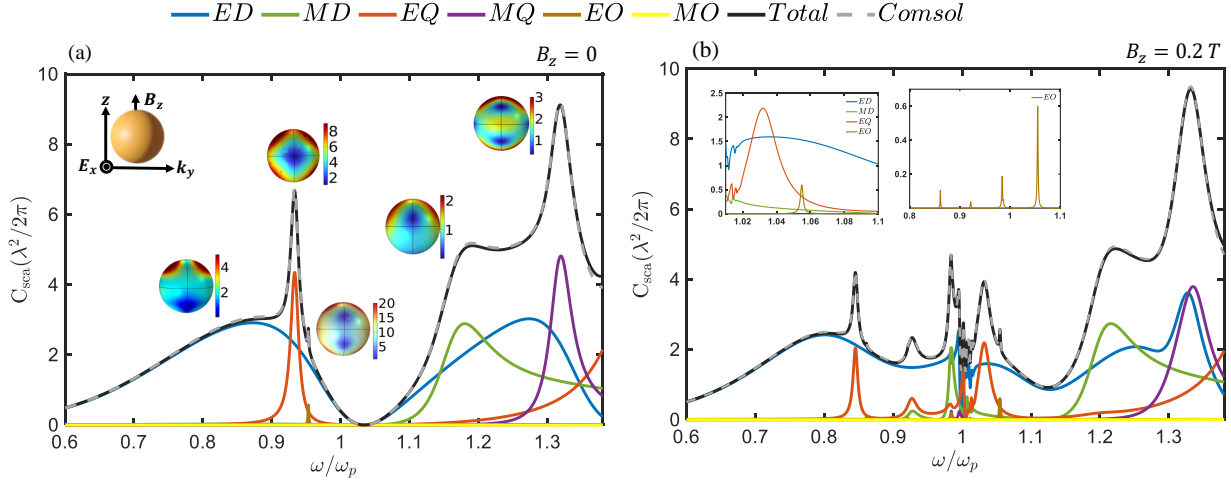


Figure S2: The scattering characteristics of the spherical InSb antenna with the radius  $r = 30\mu\text{m}$  under  $x$ -polarized plane wave illumination with the wavevector  $k_y$ , (a) in the absence and (b) presence of the applied magnetic field. (a) The total SCS of the antenna indicates five resonance peaks arising from the contribution of dominant ED, MD, EQ, MQ, and EO modes. The insets demonstrate the antenna's instantaneous normalized electric field distributions corresponding to the total SCS maxima, further clarifying the nature of electromagnetic resonant modes. (b) The scattering characteristics of the antenna are modified upon magnetization where the Zeeman splitting effect makes visibility from invisibility around  $\omega/\omega_p = 1$ . The insets specifically focus on the SCS of the magnetized antenna in the ENZ region. Here, the high- $Q$  multiband EO resonant modes significantly influence the antenna's scattering response, thereby enhancing light manipulation.

Figure S2 shows the SCS of the InSb antenna, allowing us to identify the electromagnetic resonant modes excited in the system. The spectral response of the SCS is divided into three specific regions corresponding to InSb's dielectric permittivity shown in Fig. S1(a). The induced electric conductive current excites a broad ED, a narrow EQ, and an ultra-narrow linewidth EO with a very small magnitude corresponding to negative values of InSb's permittivity to realize a plasmonic antenna in the studied frequency range of  $\omega/\omega_p < 1$ . The total SCS of the antenna at frequencies slightly higher than  $\omega_p$  nearly vanishes to provide a transparent region associated with near-zero values of InSb permittivity. An induced circular displacement current is excited inside the antenna at higher frequencies, so the total SCS also has contributions from magnetic dipole (MD) and magnetic quadrupole (MQ) modes. The concurrent support of multipolar electric and magnetic resonances realizes a dielectric antenna associated with positive real parts of InSb permittivity. The scattering response of the antenna is dramatically enhanced in the transparent region under a biased magnetic field due to the contribution of the splitting EQ and EO resonant modes, as shown in Fig. S2(b).

## B.2 Hybrid Antenna

In this section, we scrutinize the scattering response of the hybrid antenna excited by a linearly  $z$ -polarized plane wave impinging along the  $x$ -axis, as shown in Fig. S3. The antenna is made of a lower InSb layer and an upper Si layer with a radius of  $35\mu\text{m}$  and a height of  $8\mu\text{m}$  and  $80\mu\text{m}$  respectively. Under zero magnetization, the multipolar decomposition of SCS reveals a resonance with a high  $Q$  factor in the spectral interval around  $\omega/\omega_p = 1.22$ , corresponding to contributions of the dominant MO mode, which is splitted into two resonant modes with high- $Q$  factors upon weak magnetization. Insets demonstrate the normalized instantaneous electric field distributions of the total SCS maxima, allowing us to elucidate how the incident wave resonantly interacts with the antenna. The anti-parallel electric field's polarizability at opposite sides of the dielectric cylinder induces a circular displacement current, leading to a narrow linewidth MO resonance inside the particle.

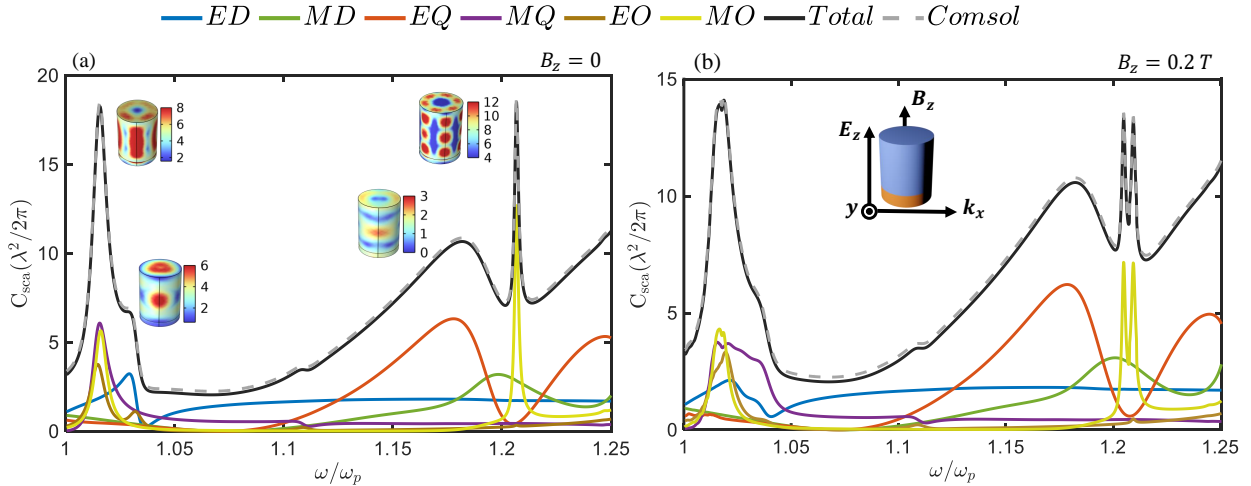


Figure S3: The SCS of the hybrid cylindrical antenna under  $z$ -polarized plane wave illumination with the wavevector  $k_x$  (a) in the absence and (b) presence of the applied static magnetic field. The scattering response of the antenna supports all multipole moments across the studied spectral range in which the contribution of the MO mode is significant and experiences the Zeeman splitting effect upon magnetization, leading to the splitted MO resonant modes, as shown in panel (b). The upper part of the antenna is made of a Si layer with the height and radius of  $80$  and  $35\mu\text{m}$ , respectively. InSb layer comprises the lower part of the antenna with the height and radius of  $8$  and  $35\mu\text{m}$ , respectively. Insets show the instantaneous normalized electric field distributions around the antenna corresponding to the total SCS maxima.

## S3 Optimization Method Algorithm

Our methodology employs stochastic gradient descent (SGD) to refine our model's parameters iteratively. SGD fine-tunes the CNN's weights and biases by minimizing the MSE loss. Given the intricate high-dimensional nature of the coupled system features, we use a genetic algorithm to pinpoint the most relevant feature subset. This algorithm evolves a population of feature sets over multiple iterations, leveraging crossover and mutation techniques. The effectiveness of each feature set is assessed through the accuracy of CNN's predictions.

In our validation, we conduct rigorous tests on a contemporary dataset encompassing diverse antenna systems. Our deep learning model outperforms conventional regression techniques. Furthermore, the genetic algorithm adaptly discerns the paramount features crucial for precise decay rate prediction. Overall, integrating deep learning with genetic algorithm-driven feature selection presents a significant advancement in addressing challenges in coupled emitter-antenna systems (See. Algorithm 1).

---

**Algorithm 1** Enhanced Deep Learning and Genetic Algorithms for Radiative Decay Rate Prediction
 

---

```

1: Data Preprocessing:
2: Normalize spatial coordinates  $(x, y, z)$ 
3: Apply one-hot encoding for frequency and applied magnetic field
4: Neural Network Initialization:
5: Set up neural network architecture with random weights and biases
6: Genetic Algorithm Parameters:
7: Set population size  $P$ , number of generations  $G$ , and mutation rate  $M$ 
8: Initialize population of feature sets  $F$  with  $P$  individuals
9: Deep Learning Training:
10: Define the number of epochs and learning rate
11: for each epoch do
12:   Compute predicted radiative decay rate  $\hat{Y}$ 
13:   Compute MSE loss:  $MSE = \frac{1}{n} \sum_{i=1}^n (Y_i - \hat{Y}_i)^2$ 
14:   Update model parameters via optimizer
15: end for
16: Genetic Optimization:
17: for generation  $g = 1$  to  $G$  do
18:   Evaluate fitness of each feature set  $f \in F$  using the neural network
19:   Select best-performing individuals for mating pool  $MatingPool$ 
20:   Populate  $NewF$  by applying genetic operations on  $MatingPool$ 
21:   for each feature set  $f \in NewF$  do
22:     if random value  $< M$  then
23:       Introduce mutation to  $f$ 
24:     end if
25:   end for
26:   Update population:  $F \leftarrow NewF$ 
27: end for
28: Optimal Features:
29: Select feature set with the topmost fitness value from the final population
30: Final Prediction:
31: Predict radiative decay rate using the selected feature set

```

---

## References

- [1] KH Drexhage. Influence of a dielectric interface on fluorescence decay time. *Journal of luminescence*, 1:693–701, 1970.
- [2] Edward M Purcell, Henry Cutler Torrey, and Robert V Pound. Resonance absorption by nuclear magnetic moments in a solid. *Physical review*, 69(1-2):37, 1946.
- [3] Roy J Glauber and M Lewenstein. Quantum optics of dielectric media. *Physical Review A*, 43(1):467, 1991.
- [4] Stefano Paesani, Massimo Borghi, Stefano Signorini, Alexandre Maïnos, Lorenzo Pavesi, and Anthony Laing. Near-ideal spontaneous photon sources in silicon quantum photonics. *Nature communications*, 11(1):1–6, 2020.
- [5] Sumin Choi, Toan Trong Tran, Christopher Elbadawi, Charlene Lobo, Xuewen Wang, Saulius Juodkazis, Gediminas Seniutinas, Milos Toth, and Igor Aharonovich. Engineering and localization of quantum emitters in large hexagonal boron nitride layers. *ACS applied materials & interfaces*, 8(43):29642–29648, 2016.
- [6] Ruoxi Wang, Michio Ikezawa, Yoshiki Sakuma, Hiroyuki Takeda, Naoki Ikeda, Yoshimasa Sugimoto, Kazuaki Sakoda, Yuuta Yamada, and Yasuaki Masumoto. Enhanced spontaneous emission rates for single isoelectronic luminescence centers in photonic crystal cavities. *ACS Photonics*, 7(2):321–326, 2020.

- [7] David Arbel, Nikolai Berkovitch, Amir Nevet, Andrea Peer, Shimon Cohen, Dan Ritter, and Meir Orenstein. Light emission rate enhancement from inp mqw by plasmon nano-antenna arrays. *Optics Express*, 19(10):9807–9813, 2011.
- [8] Bruno Romeira and Andrea Fiore. Purcell effect in the stimulated and spontaneous emission rates of nanoscale semiconductor lasers. *IEEE Journal of Quantum Electronics*, 54(2):1–12, 2018.
- [9] Fuzhi Wang, Shengli Jin, Wenda Sun, Jingting Lin, Baogui You, Yang Li, Bing Zhang, Tasawar Hayat, Ahmed Alsaedi, and Zhan’ao Tan. Enhancing the performance of blue quantum dots light-emitting diodes through interface engineering with deoxyribonucleic acid. *Advanced Optical Materials*, 6(21):1800578, 2018.
- [10] Peng Yu, Ziyuan Li, Tongwei Wu, Yi-Tao Wang, Xin Tong, Chuan-Feng Li, Zhongchang Wang, Su-Huai Wei, Yunyan Zhang, Huiyun Liu, et al. Nanowire quantum dot surface engineering for high temperature single photon emission. *ACS nano*, 13(11):13492–13500, 2019.
- [11] Kasey J Russell, Tsung-Li Liu, Shanying Cui, and Evelyn L Hu. Large spontaneous emission enhancement in plasmonic nanocavities. *Nature Photonics*, 6(7):459–462, 2012.
- [12] Felicia Tam, Glenn P Goodrich, Bruce R Johnson, and Naomi J Halas. Plasmonic enhancement of molecular fluorescence. *Nano letters*, 7(2):496–501, 2007.
- [13] Javier Cambiasso, Gustavo Grinblat, Yi Li, Aliaksandra Rakovich, Emiliano Cortés, and Stefan A Maier. Bridging the gap between dielectric nanophotonics and the visible regime with effectively lossless gallium phosphide antennas. *Nano letters*, 17(2):1219–1225, 2017.
- [14] Igor Aharonovich, Dirk Englund, and Milos Toth. Solid-state single-photon emitters. *Nature Photonics*, 10(10):631–641, 2016.
- [15] Sonia Buckley, Kelley Rivoire, and Jelena Vučković. Engineered quantum dot single-photon sources. *Reports on Progress in Physics*, 75(12):126503, 2012.
- [16] Alexander Lohrmann, BC Johnson, JC McCallum, and Stefania Castelletto. A review on single photon sources in silicon carbide. *Reports on Progress in Physics*, 80(3):034502, 2017.
- [17] Edward Mills Purcell. Spontaneous emission probabilities at radio frequencies. In *Confined Electrons and Photons*, pages 839–839. Springer, 1995.
- [18] Serge Haroche, Jean-Michel Raimond, and Jonathan P Dowling. Exploring the quantum: Atoms, cavities, and photons. *American Journal of Physics*, 82(1):86–87, 2014.
- [19] Zhiyuan Qian, Lingxiao Shan, Xinchun Zhang, Qi Liu, Yun Ma, Qihuang Gong, and Ying Gu. Spontaneous emission in micro-or nanophotonic structures. *PhotonIX*, 2(1):1–35, 2021.
- [20] Faraz A Inam, Nadeem Ahmed, Michael J Steel, and Stefania Castelletto. Hyperbolic metamaterial resonator-antenna scheme for large, broadband emission enhancement and single-photon collection. *JOSA B*, 35(9):2153–2162, 2018.
- [21] Nadeem Ahmed, Saba Akhtar, and Faraz A Inam. Hyperbolic metamaterial-based metal-dielectric resonator-antenna designs for ghz photon collection rates from wide-range solid-state single-photon sources. *JOSA B*, 37(11):3469–3477, 2020.
- [22] Caner Guclu, Ting Shan Luk, George T Wang, and Filippo Capolino. Radiative emission enhancement using nano-antennas made of hyperbolic metamaterial resonators. *Applied Physics Letters*, 105(12):123101, 2014.
- [23] Nicolas Bonod. Controlling spontaneous emission with dielectric optical antennas. In *Dielectric Metamaterials*, pages 109–144. Elsevier, 2020.
- [24] Mario Agio. Optical antennas as nanoscale resonators. *Nanoscale*, 4(3):692–706, 2012.
- [25] TH Taminiau, FD Stefani, Franciscus B Segerink, and NF Van Hulst. Optical antennas direct single-molecule emission. *Nature photonics*, 2(4):234–237, 2008.
- [26] Sergei Kühn, Ulf Håkanson, Lavinia Rogobete, and Vahid Sandoghdar. Enhancement of single-molecule fluorescence using a gold nanoparticle as an optical nanoantenna. *Physical review letters*, 97(1):017402, 2006.
- [27] Pascal Anger, Palash Bharadwaj, and Lukas Novotny. Enhancement and quenching of single-molecule fluorescence. *Physical review letters*, 96(11):113002, 2006.
- [28] Hua Mi, Le Wang, Yanpei Zhang, Guangtao Zhao, and Ruibin Jiang. Control of the emission from electric and magnetic dipoles by gold nanocup antennas. *Optics Express*, 27(10):14221–14230, 2019.
- [29] Quanbo Jiang, Prithu Roy, Jean-Benoît Claude, and Jérôme Wenger. Single photon source from a nanoantenna-trapped single quantum dot. *Nano Letters*, 21(16):7030–7036, 2021.



- [30] Sina Aghili, Saeed Golmohammadi, and Aydin Amini. Proposing an on/off optical router in telecom wavelength using plasmonic tweezer. *Optics Communications*, 427:95–100, 2018.
- [31] Lavinia Rogobete, Franziska Kaminski, Mario Agio, and Vahid Sandoghdar. Design of plasmonic nanoantennae for enhancing spontaneous emission. *Optics letters*, 32(12):1623–1625, 2007.
- [32] Sven M Hein and Harald Giessen. Tailoring magnetic dipole emission with plasmonic split-ring resonators. *Physical review letters*, 111(2):026803, 2013.
- [33] Amit Raj Dhawan, Chérif Belacel, Juan Uriel Esparza-Villa, Michel Nasilowski, Zhiming Wang, Catherine Schwob, Jean-Paul Hugonin, Laurent Coolen, Benoît Dubertret, Pascale Senellart, et al. Extreme multiexciton emission from deterministically assembled single-emitter subwavelength plasmonic patch antennas. *Light: Science & Applications*, 9(1):1–9, 2020.
- [34] Pavel A Dmitriev, Denis G Baranov, Valentin A Milichko, Sergey V Makarov, Ivan S Mukhin, Anton K Samusev, Alexander E Krasnok, Pavel A Belov, and Yuri S Kivshar. Resonant raman scattering from silicon nanoparticles enhanced by magnetic response. *Nanoscale*, 8(18):9721–9726, 2016.
- [35] Masanobu Iwanaga. All-dielectric metasurfaces with high-fluorescence-enhancing capability. *Applied Sciences*, 8(8):1328, 2018.
- [36] Lin Cheng, Rasoul Alaee, Akbar Safari, Mohammad Karimi, Lei Zhang, and Robert W Boyd. Superscattering, superabsorption, and nonreciprocity in nonlinear antennas. *ACS Photonics*, 8(2):585–591, 2021.
- [37] Ehsan Mobini, Rasoul Alaee, Robert W Boyd, and Ksenia Dolgaleva. Giant asymmetric second-harmonic generation in bianisotropic metasurfaces based on bound states in the continuum. *ACS Photonics*, 8(11):3234–3240, 2021.
- [38] Sheng Liu, Aleksandr Vaskin, Salvatore Campione, Omri Wolf, Michael B Sinclair, John Reno, Gordon A Keeler, Isabelle Staude, and Igal Brener. Huygens metasurfaces enabled by magnetic dipole resonance tuning in split dielectric nanoresonators. *Nano letters*, 17(7):4297–4303, 2017.
- [39] Yang Yang, Bofeng Zhu, and Haitao Dai. Strong magnetic field enhancement and magnetic purcell effect in a dielectric disk-ring composite nanocavity. *JOSA B*, 37(3):702–708, 2020.
- [40] Brice Rolly, Betina Bebey, Sebastien Bidault, Brian Stout, and Nicolas Bonod. Promoting magnetic dipolar transition in trivalent lanthanide ions with lossless mie resonances. *Physical Review B*, 85(24):245432, 2012.
- [41] P Elli Stamatopoulou and Christos Tserkezis. Role of emitter position and orientation on silicon nanoparticle-enhanced fluorescence. *OSA Continuum*, 4(3):918–932, 2021.
- [42] H Chew. Transition rates of atoms near spherical surfaces. *The Journal of chemical physics*, 87(2):1355–1360, 1987.
- [43] Erdem Aslan. Engineering of dual-band magnetic dipole decay rate enhancement with concentric hollow nanodisk resonators. *Optical Materials*, 113:110871, 2021.
- [44] Dmitry S Filonov, Alexander E Krasnok, Alexey P Slobozhanyuk, Polina V Kapitanova, Elizaveta A Nenasheva, Yuri S Kivshar, and Pavel A Belov. Experimental verification of the concept of all-dielectric nanoantennas. *Applied Physics Letters*, 100(20):201113, 2012.
- [45] Alexander Krasnok, Stanislav Glybovski, Mihail Petrov, Sergey Makarov, Roman Savelev, Pavel Belov, Constantin Simovski, and Yuri Kivshar. Demonstration of the enhanced purcell factor in all-dielectric structures. *Applied Physics Letters*, 108(21):211105, 2016.
- [46] Davide Rocco, Aristeidis Lamprianidis, Andrey E Miroshnichenko, and Costantino De Angelis. Giant electric and magnetic purcell factor in dielectric oligomers. *JOSA B*, 37(9):2738–2744, 2020.
- [47] Grigorios P Zouros, Georgios D Kolezas, Evangelos Almpanis, and Kosmas L Tsakmakidis. Three-dimensional giant invisibility to superscattering enhancement induced by zeeman-split modes. *ACS Photonics*, 8(5):1407–1412, 2021.
- [48] Jan Chochol, Kamil Postava, Michael Čada, Mathias Vanwolleghem, Lukáš Halagačka, Jean-François Lampin, and Jaromír Pištorá. Magneto-optical properties of insb for terahertz applications. *AIP Advances*, 6(11):115021, 2016.
- [49] Lukas Novotny and Bert Hecht. *Principles of nano-optics*. Cambridge university press, 2012.
- [50] Hiba Alhalaby, Haitham Zaraket, and Maria Principe. Enhanced photoluminescence with dielectric nanostructures: A review. *Results in Optics*, 3:100073, 2021.
- [51] Comsol Software. [www.comsol.com](http://www.comsol.com).

- [52] Yuntian Chen, Torben Roland Nielsen, Niels Gregersen, Peter Lodahl, and Jesper Mørk. Finite-element modeling of spontaneous emission of a quantum emitter at nanoscale proximity to plasmonic waveguides. *Physical Review B*, 81(12):125431, 2010.
- [53] A Márquez and R Esquivel-Sirvent. Terahertz response of plasmonic nanoparticles: Plasmonic zeeman effect. *Optics Express*, 28(26):39005–39016, 2020.
- [54] Rasoul Alaei, Carsten Rockstuhl, and Ivan Fernandez-Corbaton. An electromagnetic multipole expansion beyond the long-wavelength approximation. *Optics Communications*, 407:17–21, 2018.
- [55] Mikolaj K Schmidt, Ruben Esteban, JJI Sáenz, I Suárez-Lacalle, S Mackowski, and Javier Aizpurua. Dielectric antennas—a suitable platform for controlling magnetic dipolar emission. *Optics express*, 20(13):13636–13650, 2012.
- [56] JR Lackowicz. Principles of fluorescence spectroscopy, 1999 kluwer academic.
- [57] Mikhail V Rybin, Kirill L Koshelev, Zarina F Sadrieva, Kirill B Samusev, Andrey A Bogdanov, Mikhail F Limonov, and Yuri S Kivshar. High-q supercavity modes in subwavelength dielectric resonators. *Physical review letters*, 119(24):243901, 2017.
- [58] Serkan Kiranyaz, Onur Avcı, Osama Abdeljaber, Turker Ince, Moncef Gabbouj, and Daniel J Inman. 1d convolutional neural networks and applications: A survey. *Mechanical systems and signal processing*, 151:107398, 2021.
- [59] Amirreza Ahmadnejad, Ahmad Mahmmodian Darviishani, Mohmmad Mehrdad Asadi, Sajjad Saffariyeh, Pedram Yousef, and Emad Fatemizadeh. Tacnet: Temporal audio source counting network. *arXiv preprint arXiv:2311.02369*, 2023.
- [60] Grigorios P Zouros, Georgios D Kolezas, Evangelos Almpanis, Konstantinos Baskourellos, Tomasz P Stefański, and Kosmas L Tsakmakidis. Magnetic switching of kerker scattering in spherical microresonators. *Nanophotonics*, 9(12):4033–4041, 2020.
- [61] Sina Aghili, Aydin Amini, Leyla Shirafkan Dizaj, and Ksenia Dolgaleva. Thz plasmonic metasurface based on a periodic array of insb metamolecules with narrow resonances. *Optics Communications*, 508:127805, 2022.